The Astrophysical Journal Letters, 935:L2 (5pp), 2022 August 10 https://doi.org/10.3847/2041-8213/ac8552

Ignition of Carbon Burning from Nuclear Fission in Compact Stars

C. J. Horowitz
Center for Exploration of Energy and Matter and Department of Physics, Indiana University, Bloomington, IN 47405, USA; horowit@indiana.edu
Received 2022 July 6; revised 2022 July 28; accepted 2022 July 29; published 2022 August 9

Abstract

Type Ia supernovae (SN Ia) are powerful stellar explosions that provide important distance indicators in cosmology. Recently, we proposed a new SN Ia mechanism that involves a nuclear fission chain reaction in an isolated white dwarf (WD). The first solids that form as a WD starts to freeze are actinide rich and potentially support a fission chain reaction. In this Letter, we explore thermonuclear ignition from fission heating. We perform thermal diffusion simulations and find at high densities, above about 7×10^8 g cm^{-3}, that fission heating can ignite carbon burning. This could produce an SN Ia or another kind of astrophysical transient.

Unified Astronomy Thesaurus concepts: Type Ia supernovae (1728); White dwarf stars (1799)

1. Introduction

Type Ia supernovae (SNe Ia) are great stellar explosions that provide important distance indicators in cosmology (Abbott et al. 2019; Howell 2011; Sullivan 2010). They can be observed at great distances and appear to have a standardizable luminosity that can be inferred from other observations (Riess et al. 1996; Phillips et al. 1999; Goldhaber et al. 2001; Phillips & Burns 2017; Hayden et al. 2019). This allows a precise determination of the expansion rate of the universe known as the Hubble constant. Nevertheless, there is still some uncertainty as to the SN Ia explosion mechanism and their progenitor systems.

Traditionally, SNe Ia are thought to involve the thermonuclear explosion of a C/O white dwarf (WD) in a binary system. Here the companion is either a conventional star (single-degenerate mechanism) or another WD (double-degenerate) (Wang & Han 2012; Hillebrandt et al. 2013; Ruiz-Lapuente 2014). Recently, we proposed a new SN Ia mechanism that involves a nuclear fission chain reaction igniting thermonuclear carbon burning in an isolated WD (Horowitz & Caplan 2021a, 2021b). Alternative mechanisms to ignite isolated WD include dark matter interactions (Bramante 2015; Steigerwald et al. 2022) or pycnonuclear fusion of impurities (Chiosi et al. 2015).

Our model involves three stages. In the first stage, phase separation upon crystallization produces an actinide-rich solid that could support a nuclear fission chain reaction. In a WD, melting points of the chemical elements scale as their atomic number $Z^{5/3}$. Actinides have the highest Z and may therefore condense first. The composition of the first solids is discussed in Horowitz & Caplan (2021a).

The concentration of actinides by chemical separation in a WD is similar to the formation of uranium-rich veins on earth. Not only has uranium been purified by natural processes on earth, but natural chain reactions have also occurred. The Oklo natural nuclear reactors operated 2 Gy ago in very rich uranium deposits in Africa (Gauthier-Lafaye et al. 1996; Meshik et al. 2004; Cowan 1976).

In the second stage of our model, a chain reaction occurs in a WD. Nuclear reaction network simulations of this stage were presented in Deibel et al. (2021) where it was found that the reaction proceeds very rapidly. Fertile isotopes such as ^{238}U or ^{232}Th can burn via a two-step process where a neutron is captured to produce an odd A isotope that fissions after absorbing a second neutron. As a result, a large fraction of the initial U and Th fissions produce significant heating.

In the third stage, fission heating ignites carbon burning and initiates an SN Ia or other astrophysical transient. In this Letter, we present the first simulations of this stage. We find that fission heating can initiate carbon burning if the density is high enough. For context, our mechanism is similar to a hydrogen bomb. The Classical Super is an H-bomb design that uses heat from an atomic bomb to ignite hydrogen isotopes (Ford 2015). The Classical Super likely fails because too much energy is lost to radiation. In contrast, modern weapons may use radiation to first compress the system to higher densities where there is less energy loss. Thermonuclear ignition may be easier at high densities. Therefore, we explore ignition for different WD densities.

Timmes & Woosley (1992) discuss ignition in terms of heating at least a trigger mass $M_{\rm trig}$ of material. $M_{\rm trig}$ is estimated from the mass in a sphere of radius equal to the carbon burning flame width δ. δ decreases with density roughly as $\rho^{-5/3}$ so that $M_{\rm trig}$ decreases rapidly as $\approx\rho^{-4}$. In our model, the mass of an actinide-rich crystal likely exceeds $M_{\rm trig}$ at high densities.

In Section 2 we review the results of Horowitz & Caplan (2021a) for the size of the initial actinide-rich crystal. Next, we extend the fission reaction network simulations of Deibel et al. (2021) to higher densities. We then describe our thermal diffusion simulations. Results for carbon and oxygen ignition are presented in Section 3. We end by discussing possible implications and conclude in Section 4.

2. Formalism

Actinide-rich crystallization: As a WD cools it eventually crystallizes. However just before the main C and O components start to freeze, higher-Z impurities may condense because they have much higher melting temperatures. This process is described in Horowitz & Caplan (2021a), where the crystal is assumed to grow by diffusion until a chain reaction is started

Table 1
Actinide-rich Crystal (Pit) Mass $M_{\rm pit}$ and Radius $r_{\rm pit}$ for Different Densities ρ

ρ (g cm^{-3})	$M_{\rm pit}$ (mg)	$r_{\rm pit}$ (cm)
10^8	10	3×10^{-4}
8×10^8	20	2×10^{-4}
3×10^9	30	1.3×10^{-4}

by a neutron from spontaneous fission. The crystal mass $M_{\rm pit}$ forms the fission core of our simulation, and we refer to it as the pit in analogy with nuclear weapons. $M_{\rm pit}$ is estimated by setting the time to grow by diffusion equal to the time between neutrons. Extending the analysis of Horowitz & Caplan (2021a) to other densities gives the results in Table 1. The pit mass is seen to increase slowly with density $M_{\rm pit}\propto\rho^{3/10}$.

Fission chain reaction: This crystal, if critical, will undergo a fission chain reaction. Nuclear reaction network simulations were presented in Deibel et al. (2021), see Figure 1, where the fission heating rate per baryon $\dot{S}_{\rm fis}$ was calculated, see Figure 2. The initial composition included some Pb in addition to U and Th. Pb is essentially inert during the reaction but increases the heat capacity and therefore acts to dilute the fission heating and reduce the maximum temperature. However, the composition of the initial solid is uncertain. To explore ignition most simply, we now consider a composition identical to Horowitz & Caplan (2021a) but without Pb. The composition shown in Figure 1 and the fission heating in Figure 2 is otherwise identical to Case B of Deibel et al. (2021). If Pb is present, it pushes the threshold for ignition to higher densities as discussed below.

Fusion ignition simulations: We now perform thermal diffusion simulations of ignition. Assuming a constant pressure P, the conservation of energy can be written (Timmes & Woosley 1992) as

$$\frac{\partial E}{\partial t}+P\frac{\partial}{\partial t}\left(\frac{1}{\rho_b}\right)=\frac{1}{\rho_b}\nabla\cdot\sigma\nabla T+\dot{S}_{\rm tot}, \tag{1}$$

where E is the internal energy per baryon, T the temperature, ρ_b the baryon density, σ the thermal conductivity, and $\dot{S}_{\rm tot}$ the total nuclear reaction heating rate per baryon. We expect constant pressure to be a good approximation because the flame moves subsonically and sound waves can restore the background pressure.

Our goal is to demonstrate the physics in as clear a way as possible. The simple equation of state we use is a largely degenerate, very relativistic electron gas with internal energy per baryon

$$E\approx Y_e\left(\frac{3}{4}\epsilon_F+\frac{\pi^2}{2}\frac{T^2}{\epsilon_F}\right), \tag{2}$$

Fermi energy $\epsilon_F=(3\pi^2Y_e\rho_b)^{1/3}$, and electron fraction Y_e. We use units $\hbar=c=k_b=1$. The sum of the two terms on the left-hand side of Equation (1) can be combined using the heat capacity at constant pressure $C_p=5\pi^2Y_eT/(4\epsilon_F)$, so that Equation (1) becomes

$$\frac{\partial T}{\partial t}=\frac{1}{C_p\rho_b}\nabla\cdot\sigma\nabla T+\frac{\dot{S}_{\rm tot}}{C_p}. \tag{3}$$

We directly simulate Equation (3), assuming spherical symmetry, with a simple first-order implicit scheme (Koonin 1986). The thermal conductivity σ is from electron conduction where the mean free path is limited by electron–ion scattering. This scattering depends on the average charge $\langle Z\rangle$ of the ions, which decreases as ions fission; see Figure 2. To evaluate σ, we use the simple formulas of Yakovlev & Urpin (1980). The highly charged ions reduce σ and somewhat slow thermal diffusion. The initial conditions involve an actinide-rich crystal for $0\leqslant r\leqslant r_{\rm pit}$ and a 50/50% (by mass) C/O liquid for $r_{\rm pit}<r\leqslant r_{\rm grid}$ (except where an O/Ne/Mg composition is noted). Typically, $r_{\rm grid}=2\times10^{-3}$ to 4×10^{-3} cm. The initial temperature T_i is uniform across the grid and equal to the crystallization temperature of the actinide mixture $\approx$3 keV. The boundary conditions are $\partial T(r,\,t)/\partial r|_{r=0}=0$ and $T(r_{\rm grid},\,t)=T_i$. Simulations typically use a time step of 10^{-15} s and a uniform grid spacing of 2×10^{-6} cm. Simulations with smaller time steps and/or grid spacing often yield very similar results.

The nuclear heating $\dot{S}_{\rm tot}=\dot{S}_{\rm fis}+\dot{S}_{\rm fus}$ comes from both fission $\dot{S}_{\rm fis}$ and fusion $\dot{S}_{\rm fus}$. For $r\leqslant r_{\rm pit}$, $\dot{S}_{\rm fis}$ is taken from fission reaction simulations such as those shown in Figures 1 and 2. Because the fission chain reaction does not depend strongly on temperature, nuclear network simulations are run first and then the results simply used in thermal diffusion simulations. We note the total fission energy $S_{\rm fis}$ for the simulation in Figure 2 is $\int dt\dot{S}_{\rm fis}(t)=0.679$ MeV/baryon.

To estimate $\dot{S}_{\rm fus}$ we calculate the rate of $C+C$ fusion using the REACLIB database (Cyburt et al. 2010) and include strong screening. Using the rate from Yakovlev et al. (2006) instead yields a slightly higher threshold density for carbon ignition. $C+C$ fusion produces a number of reaction products and these undergo secondary reactions. Careful reaction network simulations in Calder et al. (2007) determined the total energy released during carbon burning to be $\Delta E=3.5\times10^{17}$ erg g^{-1} or 0.362 MeV baryon^{-1} at 8×10^8 g cm^{-3} (P200 network in Table 2 of Calder et al. 2007). For simplicity, we calculate $\dot{S}_{\rm fus}$ by assuming each $C+C$ fusion releases $Q_{\rm eff}=(24/0.5)\Delta E=17.4$ MeV. Here, there are 24 nucleons per $C+C$ fusion and only 0.5 of the fuel is carbon. This approximation can be checked by full reaction network simulations. If $Q_{\rm eff}$ is somewhat smaller, the threshold density for ignition may increase somewhat.

3. Results

Figure 3 shows temperature T versus radius r for four thermal diffusion simulations. The simulation at a low density of 2×10^8 g cm^{-3} shown in Figure 3(a) fails to ignite. Here $r_{\rm pit}=3\times10^{-4}$ cm. During the fission chain reaction, T rises so rapidly that there is only minimal thermal diffusion. However, over longer times this heat simply diffuses away without initiating carbon burning.

At a density of 4×10^8 g cm^{-3}, ignition is possible if $M_{\rm pit}$ is large. This is shown in Figure 3(b) where a carbon flame is started that burns to the right (off the edge of the figure). However, $r_{\rm pit}=6\times10^{-4}$ cm and $M_{\rm pit}=0.36$ g. This is larger than the 10–20 mg suggested in Table 1. We conclude that ignition may be possible at this density, but only if $M_{\rm pit}$ is large. If $r_{\rm pit}$ is much less than 6×10^{-4} cm, the simulation fails to ignite.

Figure 3(c) shows carbon ignition for a simulation with $r_{\rm pit}=1.7\times10^{-4}$ cm at $\rho=8\times10^8$ g cm^{-3}. At this density, $M_{\rm pit}=16$ mg is consistent with Table 1 so ignition may be likely. If $r_{\rm pit}$ is somewhat larger than 1.7×10^{-4} cm, ignition

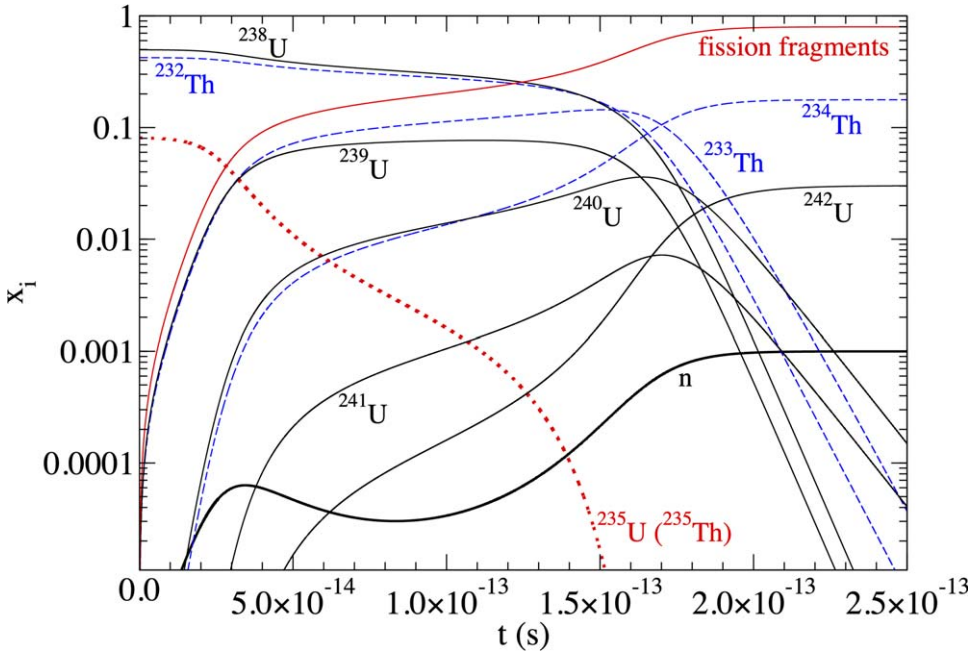

Figure 1. Abundance of U and Th isotopes (by mass) vs. time during fission chain reaction at a density $\rho = 8 \times 10^8$ g cm^{-3}. Adapted from Case B of Deibel et al. (2021).

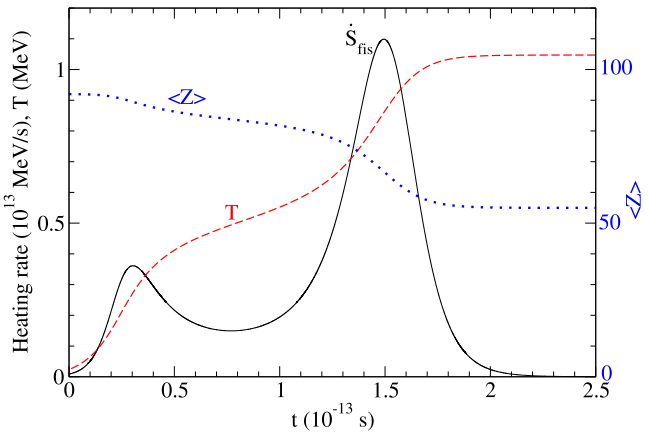

Figure 2. Fission heating rate per baryon $\dot{S}_{\rm fis}$ vs. time (black solid curve) at $\rho = 8 \times 10^8$ g cm^{-3}. The red dashed curve shows the temperature at $r = 0$ of the thermal diffusion simulation shown in Figure 3(c). The blue dotted curve shows the average charge $\langle Z \rangle$ of ions in the pit, to be read from the right-hand scale.

can take place at somewhat lower densities approximately $\geqslant 6 \times 10^8$ g cm^{-3}.

The nuclear fission chain reaction in Figures 1 and 2 emits a total fission heating of 0.679 MeV per nucleon. The fission energy released could be less if a smaller fraction of the actinides fission. Alternatively, nonfissioning impurities such as Pb that dilute the fission energy over more nucleons could be present. To explore this we multiply the fission heating rate in Figure 2 by different time-independent constants and find the total fission energy necessary for ignition at a given density; see Table 2. The fission energy required decreases from 0.66 to 0.19 MeV/nucleon as the density increases from 6×10^8 to 4×10^9 g cm^{-3}. For simplicity, all of the simulations on which Table 2 is based used $r_{\rm pit} = 3 \times 10^{-4}$ cm.

Oxygen ignition is difficult but appears possible at high densities. Figure 3(d), at a density of 5×10^9 g cm^{-3}, shows oxygen ignition. Again we use the REACLIB rates Cyburt et al. (2010). The initial composition is 60%/30%/10% O/Ne/Mg by mass, $r_{\rm pit} = 2 \times 10^{-4}$ cm, and $T_i = 7$ keV. We somewhat arbitrarily use an effective energy release of $Q_{\rm eff} =$ 16.4 MeV per O+O fusion. This is estimated from the Si-rich final composition in Figure 4(b) of Timmes & Woosley (1992). Note that the system reaches a higher temperature $T \approx 1.5$ MeV after the fission chain reaction. This is because, at very high densities, the system is more degenerate, and the heat capacity is lower. In all of the simulations shown in Figure 3, the fission energy release is 0.679 MeV/nucleon. It is possible that a very massive O/Ne star, near the Chandrasekhar mass, could experience a thermonuclear runaway via our mechanism. In contrast, an O/Ne WD might undergo electron-capture-induced collapse when it accretes matter from a companion.

4. Discussion and Conclusions

Electron capture and fission: The threshold density for electron capture, $e + {}^{235}\mathrm{U} \rightarrow {}^{235}\mathrm{Pa} + \nu_e$ is 9.2×10^7 g cm^{-3} (assuming $Y_e \approx 0.5$). This may be followed by $e + {}^{235}\mathrm{Pa} \rightarrow {}^{235}\mathrm{Th} + \nu_e$ with a threshold of 2.0×10^8 g cm^{-3}. Thus, the original ^{235}U may be in the form of ^{235}Th in the dense stellar interior. ^{235}Th with an even number of protons and an odd number of neutrons (like ^{235}U) may be fissile and have a significant cross section for neutron-induced fission. In the laboratory ^{235}Th beta decays so its fission cross section may not have been measured. We note that the single neutron separation energy of ^{236}Th is 5.9 MeV. This is the energy available for n+^{235}Th fission and is significantly larger than the 4.8 MeV single n separation energy of ^{239}U. If ^{235}Th does have a significant fission cross section, although somewhat smaller than for ^{235}U, reaction network simulations such as in Figure 1 still find comparable fission heating provided the initial ^{235}Th enrichment compared to ^{238}U+^{235}Th is somewhat higher than the 14% assumed in Figure 1.

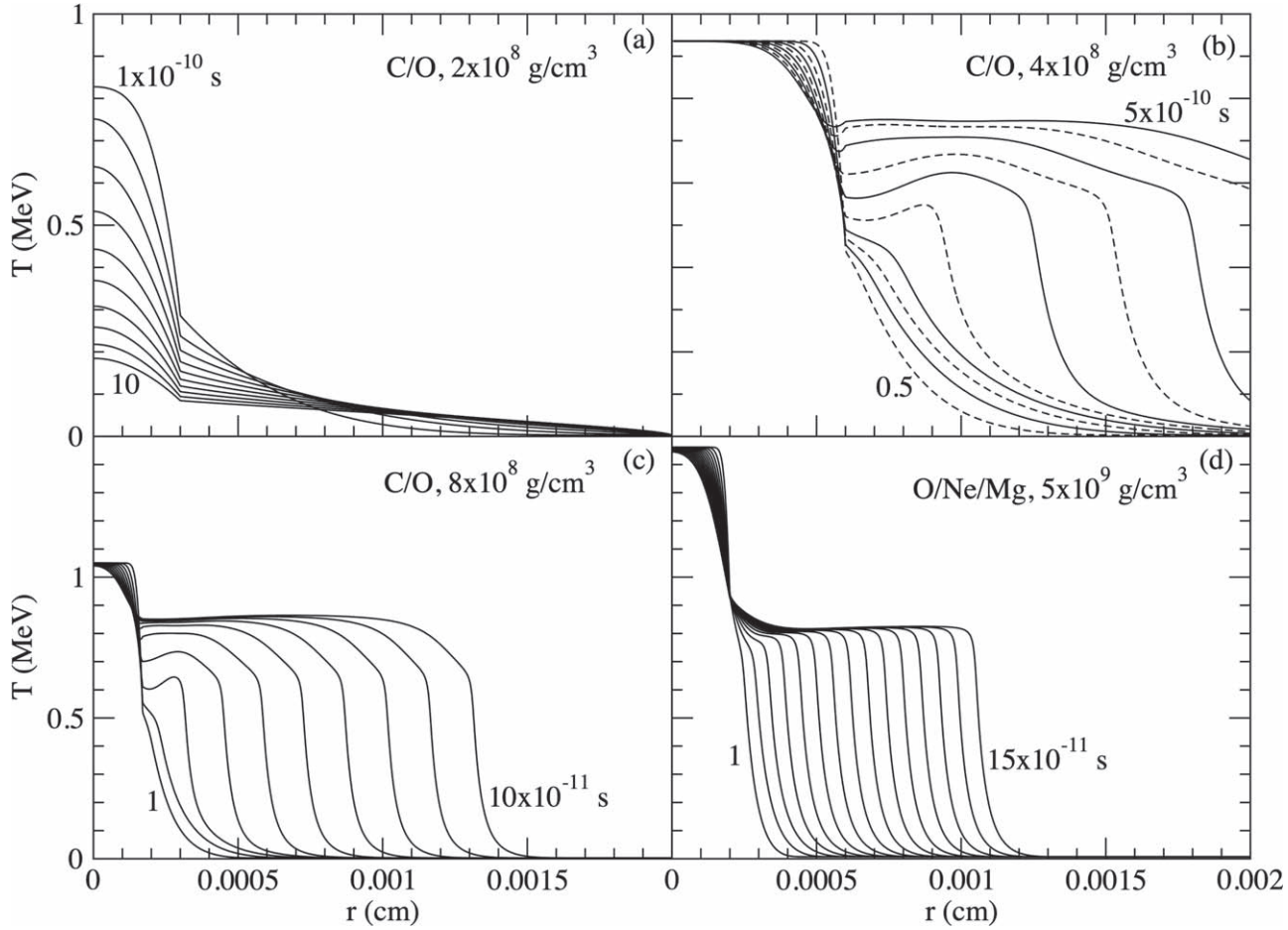

Figure 3. Temperature T vs. radius r of thermal diffusion simulations. (a) Low-density simulation that fails to ignite. Contours are shown every 10^{-10} s, top to bottom. (b) Medium-density simulation with a large $r_{\rm pit} = 6 \times 10^{-4}$ cm. Contours are shown every 0.5×10^{-10} s, bottom to top. (c) Simulation with $r_{\rm pit} = 1.7 \times 10^{-4}$ cm. Contours are shown every 10^{-11} s left to right. (d) O/Ne/Mg simulation at high density. Contours are shown every 10^{-11} s, left to right.

Table 2
Minimum Total Fission Heating $S_{\rm fis}$ Necessary for Carbon Ignition at a Given Density ρ

ρ (g cm^{-3})	$S_{\rm fis}$ (MeV/nucleon)
6×10^8	0.66
8×10^8	0.53
1×10^9	0.46
2×10^9	0.29
3×10^9	0.22
4×10^9	0.19

Alpha decay lifetimes: Uranium α decays with a 700 My half-life for ^{235}U and 4.5 Gy for ^{238}U. However, the Q value (energy released) for the α decay of ^{235}Th is smaller than that for ^{235}U, so the alpha decay systematics of Viola & Seaborg (1966) suggest ^{235}Th will have a much longer half-life. In a dense star, ^{235}Th should be effectively stable. Over long time periods, ^{238}U will still decay. As a result, the enrichment of ^{235}Th compared to ^{238}U will actually increase with time. This could make a fission chain reaction more likely.

Chandrasekhar limit: The fission mechanism does not explicitly involve the Chandrasekhar-mass limit. Nevertheless, the high density required for ignition limits the mechanism to nearly Chandrasekhar mass WD, and this might naturally produce transients of similar luminosities.

Ignition: We have an explicit simulation of ignition. We predict ignition at a single nearly central point in a very massive WD. Nucleation of an actinide-rich crystal is expected first in the highest-density region, and this should happen near, but perhaps not exactly at, the star's center. Ignition takes place in a cold star. Unlike in a conventional single-degenerate model, there is no period of carbon simmering before ignition. Ignition produces a deflagration. This might turn into a detonation later. Hydrodynamic simulations of the SN or other astrophysical transient that might follow this cold ignition should be performed. It is possible that these simulations, with ignition densities above 4×10^8 g cm^{-3}, will reproduce a reasonable typical SN Ia composition (Thielemann et al. 2004).

Ultramassive WD: One way to form ultramassive WDs with C/O cores is through mergers (Hollands et al. 2020). In our model, the SN would not occur during or shortly after the merger. Instead, it would occur some time later when the massive star formed in the merger had cooled (Camisassa et al. 2022) so that actinide crystallization could start. This is at about twice the temperature of C/O crystallization (Horowitz & Caplan 2021a). This mechanism might be related to somewhat of a hybrid between single-degenerate and double-degenerate models. Like the double-degenerate model, it would involve the merger of two WDs. Like the single-degenerate model, it would involve a deflagration ignition in a nearly Chandrasekhar-mass WD. An observable signature of our mechanism could be no detectable

gravitational-wave signal in a space-based detector such as DECIGO (Kawamura et al. 2021) (because the merger happened in the past) along with the lack of an observable ex-companion star (Schaefer & Pagnotta 2012).

In conclusion, we have performed thermal diffusion simulations of thermonuclear ignition following a natural nuclear fission chain reaction. We find that carbon ignition is possible at high densities. This could initiate an SN Ia or other astrophysical transient.

We thank Ed Brown, Ezra Booker, Alan Calder, Matt Caplan, Alex Deibel, Erika Holmbeck, Wendell Misch, Matthew Mumpower, Witek Nazarewicz, Rolfe Petschek, Catherine Pilachowski, Tomasz Plewa, and Rebecca Surman for helpful discussions. This work was performed in part at the Aspen Center for Physics, which is supported by National Science Foundation grant PHY-1607611. This research was supported in part by the US Department of Energy Office of Science Office of Nuclear Physics grants DE-FG02-87ER40365 and DE-SC0018083 (NUCLEI SCIDAC).

ORCID iDs

C. J. Horowitz https://orcid.org/0000-0001-7271-9098

References

Abbott, T. M. C., Allam, S., Andersen, P., et al. 2019, ApJL, 872, L30
Bramante, J. 2015, PhRvL, 115, 141301
Calder, A. C., Townsley, D. M., Seitenzahl, I. R., et al. 2007, ApJ, 656, 313
Camisassa, M. E., Althaus, L. G., Koester, D., et al. 2022, MNRAS, 511, 5198
Chiosi, E., Chiosi, C., Trevisan, P., Piovan, L., & Orio, M. 2015, MNRAS, 448, 2100
Cowan, G. A. 1976, SciAm, 235, 36
Cyburt, R. H., Amthor, A. M., Ferguson, R., et al. 2010, ApJS, 189, 240
Deibel, A., Caplan, M. E., & Horowitz, C. J. 2021, arXiv:2109.14714
Ford, K. W. 2015, Building the H bomb (Singapore: World Scientific)
Gauthier-Lafaye, F., Holliger, P., & Blanc, P.-L. 1996, GeCoA, 60, 4831
Goldhaber, G., Groom, D. E., Kim, A., et al. 2001, ApJ, 558, 359
Hayden, B., Rubin, D., & Strovink, M. 2019, ApJ, 871, 219
Hillebrandt, W., Kromer, M., Röpke, F. K., & Ruiter, A. J. 2013, FrPhy, 8, 116
Hollands, M. A., Tremblay, P. E., Gänsicke, B. T., et al. 2020, NatAs, 4, 663
Horowitz, C. J., & Caplan, M. E. 2021a, PhRvL, 126, 131101
Horowitz, C. J., & Caplan, M. E. 2021b, arXiv:2107.03568
Howell, D. A. 2011, NatCo, 2, 350
Kawamura, S., Ando, M., Seto, N., et al. 2021, PTEP, 2021, 05A105
Koonin, S. E. 1986, PhT, 39, 88
Meshik, A. P., Hohenberg, C. M., & Pravdivtseva, O. V. 2004, PhRvL, 93, 182302
Phillips, M. M., & Burns, C. R. 2017, in Handbook of Supernovae, ed. A. W. Alsabti & P. Murdin (Cham: Springer), 2543
Phillips, M. M., Lira, P., Suntzeff, N. B., et al. 1999, AJ, 118, 1766
Riess, A. G., Press, W. H., & Kirshner, R. P. 1996, ApJ, 473, 88
Ruiz-Lapuente, P. 2014, NewAR, 62-63, 15
Schaefer, B. E., & Pagnotta, A. 2012, Natur, 481, 164
Steigerwald, H., Marra, V., & Profumo, S. 2022, PhRvD, 105, 083507
Sullivan, M. 2010, LNP, 800, 59
Thielemann, F. K., Brachwitz, F., Höflich, P., Martinez-Pinedo, G., & Nomoto, K. 2004, NewAR, 48, 605
Timmes, F. X., & Woosley, S. E. 1992, ApJ, 396, 649
Viola, V., & Seaborg, G. 1966, J. inorg. nucl, 28, 741
Wang, B., & Han, Z. 2012, NewAR, 56, 122
Yakovlev, D. G., Gasques, L. R., Afanasjev, A. V., Beard, M., & Wiescher, M. 2006, PhRvC, 74, 035803
Yakovlev, D. G., & Urpin, V. A. 1980, SvA, 24, 303